



High harmonic generation in fullerene moleculesH. K. Avetissian, A. G. Ghazaryan , and G. F. Mkrtchian **Centre of Strong Fields Physics, Yerevan State University, 0025 Yerevan, Armenia*

(Received 11 April 2021; revised 13 September 2021; accepted 15 September 2021; published 27 September 2021)

Using dynamical Hartree-Fock mean-field theory, we study the high harmonic generation (HHG) in the fullerene molecules C_{60} and C_{70} under strong pump wave driving. We consider a strong-field regime and show that the output harmonic radiation exhibits multiple plateaus, whose borders are defined by the molecular excitonic lines and cutoff energies within each plateau scale linearly with the field strength amplitude. In contrast to atomic cases for the fullerene molecule, with the increase of the pump wave photon energy the cutoff harmonic energy is increased. We also show that with the increase of the electron-electron interaction energy overall the HHG rate is suppressed. We demonstrate that the C_{70} molecule shows richer HHG spectra and a stronger high harmonic intensity than the C_{60} .

DOI: [10.1103/PhysRevB.104.125436](https://doi.org/10.1103/PhysRevB.104.125436)**I. INTRODUCTION**

An intense light interaction with a quantum system can excite the system's electrons towards extreme nonequilibrium states during a fraction of its cycle [1,2]. Excited by the wave field and subjected to the internal forces inside the system, the electrons emit coherent electromagnetic (EM) radiation that can contain from tens to many hundreds of harmonics of an incident light [3,4]. This is one of the fundamental processes in the intense laser-matter interaction called high harmonic generation (HHG) [5]. The HHG process in atoms or molecules with the three-step model [6] explanation is a well-demonstrated method for producing coherent extreme ultraviolet radiation. The coherent spectrum of HHG implies access to the extreme time resolution of the underlying quantum dynamics that opens the way for attosecond physics [7,8] and ultrafast imaging methods for emitters themselves. In particular, using HHG spectroscopy one can reconstruct the crystal potential [9], observe Mott [10] and Peierls [11] transitions, and retrieve the band structure [12,13].

For HHG it is crucial to increase HHG conversion efficiency and to extend the harmonics cutoff [14]. Specifically, the conversion efficiency of the HHG process strongly depends on the density of emitters and the density of states of emitters. The use of molecular systems, clusters, and crystals can significantly increase the harmonic intensity by utilizing multiple excitation channels [15–17]. Thus, in the last decade, there has been a growing interest to extend HHG to crystals [18–26] and two-dimensional nanostructures, such as semimetallic graphene [27–38], semiconductor transition metal dichalcogenides [39,40], and dielectric hexagonal boron nitride [41]. Currently, this is a new growing research field—extreme nonlinear optics of nanostructured materials.

Among the variety of nanostructured materials, carbon allotropes play a central role. The discovery of fullerene C_{60}

[42] through laser evaporation of graphite and its synthesis in macroscopic amounts [43] triggered the study of many other carbon nanostructures, such as carbon nanotubes [44], graphene, and its derivatives [45]. Currently, carbon nanomaterials are promising materials for many applications, and in particular for extreme nonlinear optics. Being a member of the carbon allotropes, a strong HHG from fullerene molecules is expected. Experimentally, in Refs. [46,47] is reported a strong harmonic signal from C_{60} plasma. Theoretical works predicted a strong HHG from a C_{60} molecule [48–50] and solid C_{60} [51]. The theoretical analyses in Refs. [48–50] are dominated by a single-particle picture, but it is unclear how the electron-electron Coulomb interaction leaves its mark on HHG and subcycle electronic response in these materials. In addition, in [48], moderately strong fields were considered, and excitonic lines were termed as noninteger harmonics. However, these intrinsic exciton lines are the result of Raman scattering of light, not harmonic radiation. Another problem is how the symmetry groups of the most abundant fullerenes C_{60} and C_{70} , namely, the icosahedron group and the dihedral group, affect the HHG process in these materials.

In the present work, we develop a microscopic theory of a fullerene molecule nonlinear interaction with strong EM radiation of linear polarization taking into account electron-electron interaction (EEI). In particular, we consider C_{60} and C_{70} molecules as the most abundant examples of fullerene molecules with different point-group symmetries. By means of the dynamical Hartree-Fock approximation, we reveal the general and basal structure of the HHG spectrum and its relation to the molecular excitations.

The paper is organized as follows. In Sec. II, the considering model with the Hamiltonian in the tight-binding approximation and the master equation for the density matrix are presented. In Sec. III, we present the calculated HHG spectra and examine its fundamental structure. Finally, the conclusions are given in Sec. IV.

*mkrтчian@ysu.am

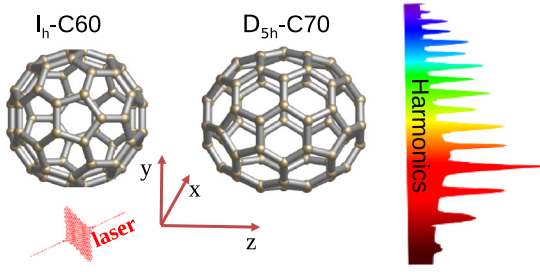


FIG. 1. A sketch of the interaction geometry with schematic structures of C_{60} and C_{70} .

II. THE TIGHT-BINDING HAMILTONIAN AND THE MASTER EQUATION FOR THE DENSITY MATRIX

Let a fullerene molecule, C_{60} or C_{70} , interact with strong coherent EM radiation that results in HHG. A sketch of the interaction geometry with an incident wave, output harmonics, and schematic structures of C_{60} and C_{70} is shown in Fig. 1. The C_{60} molecule is invariant under the inversion with respect to the center of mass and has icosahedral (I_h) point-group symmetry. The C_{70} molecule has pentagonal (D_{5h}) point-group symmetry. The z axis is chosen along the fivefold rotation axes. This means that the C_{70} molecule is mapped onto itself at $(x, y, z) \rightarrow (x, y, -z)$.

We assume neutral fullerene molecules, which will be described in the scope of the tight-binding theory where the interball hopping is much smaller than the on-ball hopping, and EEI is described in the extended Hubbard approximation [52–55]. Hence, the total Hamiltonian reads

$$\hat{H} = \hat{H}_0 + \hat{H}_{\text{int}}, \quad (1)$$

where

$$\hat{H}_0 = - \sum_{\langle i,j \rangle \sigma} t_{ij} c_{i\sigma}^\dagger c_{j\sigma} + \frac{U}{2} \sum_{i\sigma} n_{i\sigma} n_{i\bar{\sigma}} + \frac{1}{2} \sum_{\langle i,j \rangle} V_{ij} n_i n_j \quad (2)$$

is the free fullerene Hamiltonian. Here $c_{i\sigma}^\dagger$ creates an electron with the spin polarization $\sigma = \{\uparrow, \downarrow\}$ at site i ($\bar{\sigma}$ is the opposite to σ spin polarization), and $\langle i, j \rangle$ runs over all the first nearest-neighbor hopping sites with the transfer energy t_{ij} . The density operator is $n_{i\sigma} = c_{i\sigma}^\dagger c_{i\sigma}$, and the total electron density for site i is $n_i = n_{i\uparrow} + n_{i\downarrow}$. The second and third terms in (2) describe the EEI Hamiltonian with on-site and intersite Coulomb repulsion energies U and V_{ij} , respectively. Since the distance d_{ij} between the nearest-neighbor pairs varies over the system, we scale intersite Coulomb repulsion: $V_{ij} = V d_{\text{min}}/d_{ij}$, where d_{min} is the minimal nearest-neighbor distance. For all calculations we use the ratio $V = 0.4U$ [52,54]. In the Hamiltonian, we neglected the lattice vibrations. In the calculations, the light-matter interaction is described in the length gauge via the pure scalar potential

$$\hat{H}_{\text{int}} = e \sum_{i\sigma} \mathbf{r}_i \cdot \mathbf{E}(t) c_{i\sigma}^\dagger c_{i\sigma}, \quad (3)$$

with the elementary charge e , position vector \mathbf{r}_i , and the electric field strength $\mathbf{E}(t) = f(t)E_0\hat{\mathbf{e}}\cos\omega t$, with the frequency ω , polarization $\hat{\mathbf{e}}$ unit vector, pulse envelope $f(t) =$

$\sin^2(\pi t/\mathcal{T})$, and the pulse duration \mathcal{T} . From the Heisenberg equation one can obtain evolutionary equations for the single-particle density matrix $\rho_{ij}^{(\sigma)} = \langle c_{j\sigma}^\dagger c_{i\sigma} \rangle$. In addition, we will assume that the system relaxes at a rate γ to the equilibrium $\rho_{0ij}^{(\sigma)}$ distribution. To obtain a closed set of equations for the single-particle density matrix $\rho_{ij}^{(\sigma)} = \langle c_{j\sigma}^\dagger c_{i\sigma} \rangle$, EEI will be considered under the Hartree-Fock approximation. (Details are provided in Appendix A.) Thus, we obtain the following equation for the density matrix:

$$i\hbar \frac{\partial \rho_{ij}^{(\sigma)}}{\partial t} = \sum_k (\tau_{kj\sigma} \rho_{ik}^{(\sigma)} - \tau_{ik\sigma} \rho_{kj}^{(\sigma)}) + (V_{i\sigma} - V_{j\sigma}) \rho_{ij}^{(\sigma)} + e\mathbf{E}(t)(\mathbf{r}_i - \mathbf{r}_j) \rho_{ij}^{(\sigma)} - i\hbar\gamma(\rho_{ij}^{(\sigma)} - \rho_{0ij}^{(\sigma)}), \quad (4)$$

where $V_{i\sigma} = \sum_{j\alpha} V_{ij}(\rho_{jj}^{(\alpha)} - \rho_{0jj}^{(\alpha)}) + U(\rho_{ii}^{(\bar{\sigma})} - \rho_{0ii}^{(\bar{\sigma})})$ and $\tau_{ij\sigma} = t_{ij} + V_{ij}(\rho_{ji}^{(\sigma)} - \rho_{0ji}^{(\sigma)})$ are defined via the density matrix $\rho_{ij}^{(\sigma)}$ and its initial value.

We numerically diagonalize the tight-binding Hamiltonian \hat{H}_0 (see Appendix A) with the parameters that provide molecular orbitals close to experiment [56,57], and construct the initial density matrix $\rho_{0ij}^{(\sigma)}$ via the filling of electron states in the valence band according to the zero temperature Fermi-Dirac distribution $\rho_{0ij}^{(\sigma)} = \sum_{\mu=N/2}^{N-1} \psi_\mu^*(j)\psi_\mu(i)$, where $\psi_\mu(i)$ is the eigenstate of \hat{H}_0 .

III. RESULTS

The HHG spectrum is evaluated from the Fourier transformation $\mathbf{a}(\Omega)$ of the dipole acceleration $\mathbf{a}(t) = d^2\mathbf{d}/dt^2$. Corresponding dipole momentum is defined as $\mathbf{d}(t) = e \sum_{i\sigma} \mathbf{r}_i \rho_{ii}^{(\sigma)}(t)$. Then, for convenience, we normalize the dipole acceleration by the factor $a_0 = e\bar{\omega}^2\bar{d}$, where $\bar{\omega} = 1 \text{ eV}/\hbar$ and $\bar{d} = 1 \text{ \AA}$. The power radiated at the given frequency is proportional to $|\mathbf{a}(\Omega)|^2$.

As a first step and to verify our model, we make calculations for the parameters of Ref. [48] when EEI is neglected: $U = 0$. The corresponding spectrum for C_{60} is shown in Fig. 2. As seen from this figure, except for the low-frequency peak associated with the lattice vibration, our model completely reproduces the result of Ref. [48]. In particular, we see that above the seventh order, there are fractional harmonics. As was shown in Ref. [48], these peaks result from the intrinsic electronic excitations that present multiple electronic transitions between the molecular orbitals. As we will see below, these peaks also have imprints on the HHG spectra at stronger laser fields.

In order to clarify the main aspects of HHG in C_{60} and C_{70} for strong pump fields, we assume the excitation frequency is much smaller than the typical gap of $\sim 2 \text{ eV}$. For all further calculations the wave is assumed to be linearly polarized and the pulse duration \mathcal{T} is taken to be 20 wave cycles: $\mathcal{T} = 40\pi/\omega$. Prior to the Fourier transform, we apply a window function to the dipole acceleration (see Appendix B), to filter out noise at the beginning and at the end of the time evolution. Orienting the linearly polarized pump wave along different axes results in different harmonics spectra. The difference is essential for C_{70} . This is because for C_{70} the inversion symmetry takes

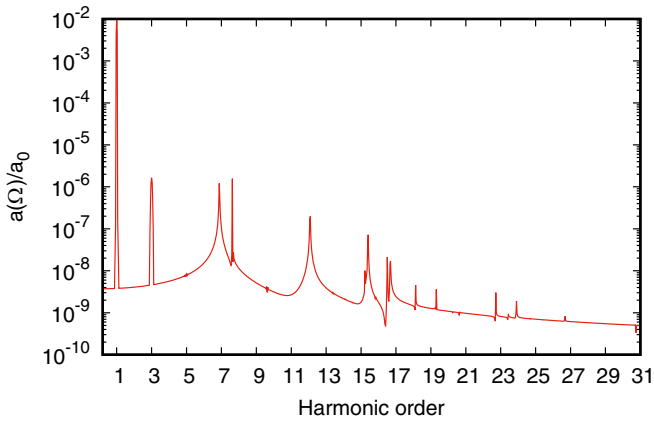


FIG. 2. The HHG spectrum in logarithmic scale via the normalized dipole acceleration Fourier transformation $a(\Omega)/a_0$ (in arbitrary units) for C_{60} . The light polarization is assumed along the x axis. The frequency is $\omega = 0.4$ eV/ \hbar , pulse duration is 32 laser cycles, and the field strength is taken to be $E_0 = 0.02$ V/ \AA . The relaxation is neglected.

place only for the fivefold rotation axes, Fig. 1. For C_{60} the HHG spectrum is almost independent of light polarization. In Figs. 3(a)–3(c), we show the HHG spectra in the strong field regime for the C_{60} molecule. For the C_{60} molecule, because of the inversion symmetry only the odd harmonics appear in the HHG spectrum. As expected, with the increase of the pump wave field strength the HHG rate and the cutoff harmonic

order increase. In Figs. 3(d)–3(f), we show the HHG spectra in the strong-field regime for the C_{70} molecule. For the latter we have both even and odd harmonics except at the z polarization of the pump wave, Fig. 3(f). The insets in Figs. 3(a) and 3(d) show low harmonics, where the difference in symmetry for C_{60} and C_{70} is clearly visible (see also Appendix A for a relatively weak field). As seen from Fig. 3, in both cases HHG spectra have a multiplateau structure that is connected with the intrinsic molecular excitations between the occupied molecular orbitals and the unoccupied molecular orbital. To show this in a more transparent way, in Fig. 3 the molecular excitonic lines are also shown. To obtain the latter, the method of coherent laser spectroscopy is used. That is, we examined the spectra of C_{60} and C_{70} upon excitation by a laser pulse of a relatively high frequency. Due to the higher energy of the photon, it is able to excite higher electron orbitals, or, in other words, electron-hole pairs. These pairs upon subsequent recombination through radiation lead to a series of peaks in the spectrum, and since our model takes into account the EEL, we call them molecular exciton lines. In particular, the lines near 2.7 and 1.7 eV for C_{60} and C_{70} , respectively, are close to the first dipole-allowed transition from the highest occupied molecular orbital to the lowest unoccupied molecular orbital. These excitonic lines were termed as noninteger harmonics in [48] and have their fingerprints in the multiplateau structure for the HHG spectra in the strong-field regime. As is seen, plateaus' borders are defined by these lines. In addition, for C_{70} there are close lines which enhance the HHG yield compared with C_{60} .

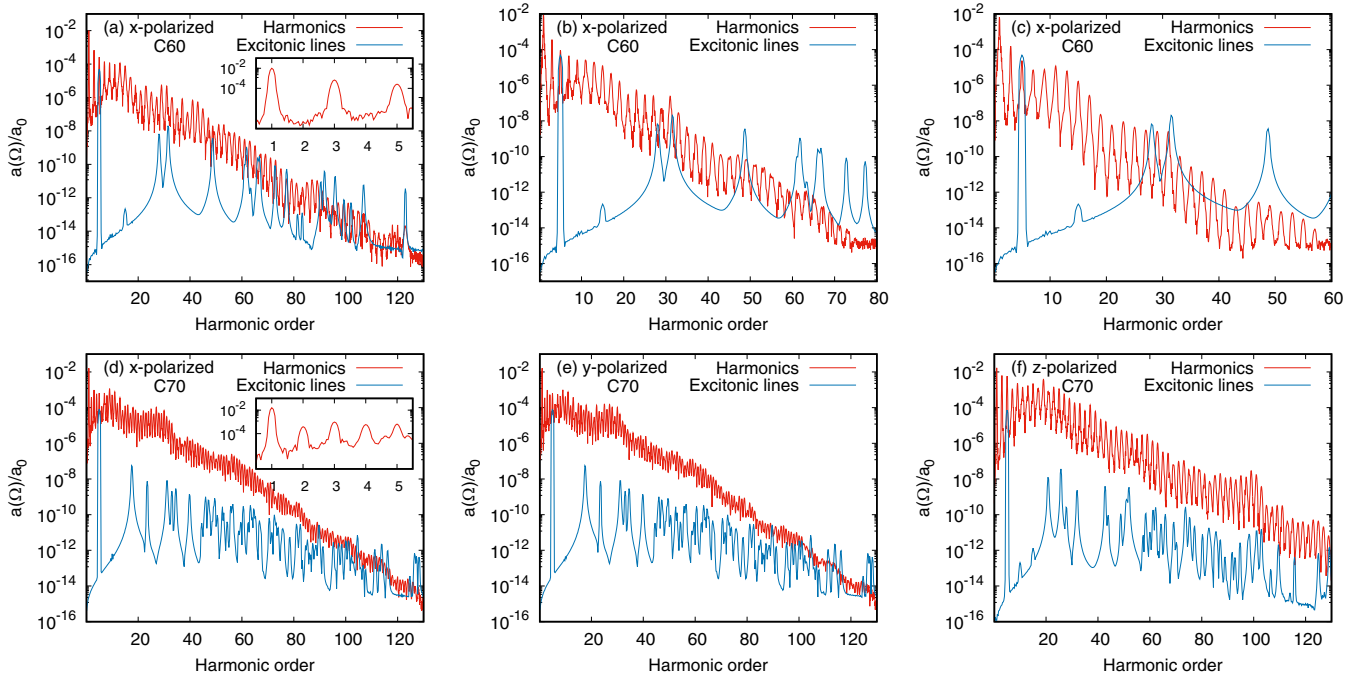


FIG. 3. The HHG spectra in the strong-field regime in logarithmic scale via the normalized dipole acceleration Fourier transformation $a(\Omega)/a_0$ (in arbitrary units) for C_{60} (a)–(c) and for C_{70} (d)–(f). The frequency is $\omega = 0.1$ eV/ \hbar . The relaxation rate is taken to be $\hbar\gamma = 50$ meV. The spectra are shown for moderate EEI energy: $U = 2$ eV. The light polarization is assumed along the x axis for C_{60} with the field strengths $E_0 = 0.5$ V/ \AA (a), $E_0 = 0.4$ V/ \AA (b), and $E_0 = 0.3$ V/ \AA (c). For C_{70} the field strength is taken to be $E_0 = 0.5$ V/ \AA and the light polarization is assumed along the different axes. The molecular excitonic lines (lower/blue curves, except the line near 0.5 eV) are also shown. The latter is obtained at the excitation of C_{60} and C_{70} with a probe laser pulse of frequency 0.5 eV/ \hbar and $E_0 = 10^{-4}$ V/ \AA . The relaxation rate is taken to be $\hbar\gamma = 0.5$ meV.

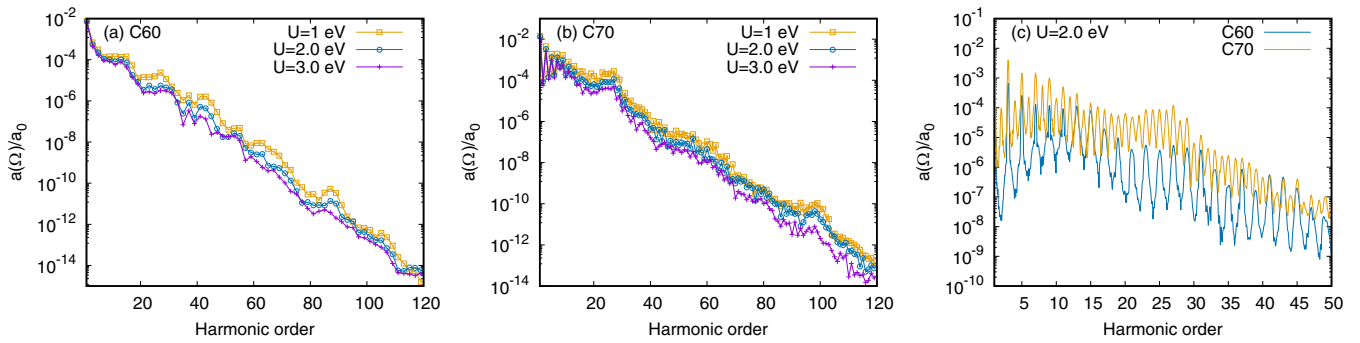


FIG. 4. The envelopes of HHG spectra (only peaks are connected) in the strong-field regime for different EEI energies in logarithmic scale via the normalized dipole acceleration Fourier transformation $a(\Omega)/a_0$ (in arbitrary units) for C_{60} (a) and C_{70} (b). The frequency is $\omega = 0.1 \text{ eV}/\hbar$ and the field strength is taken to be $E_0 = 0.5 \text{ V}/\text{\AA}$. The relaxation rate is taken to be $\hbar\gamma = 50 \text{ meV}$. In (c) we show HHG for C_{60} versus C_{70} .

Since the boundaries of the plateaus are determined by dipole-allowed multiple electronic transitions between the molecular orbitals, it can be argued that for the frequencies $\hbar\omega \ll t_{ij}$ these boundaries are almost invariant with respect to the pump wave frequency. They are determined through the intrinsic features of the free fullerene. Note also that the position of excitonic lines and relative intensities depend also on EEI. In addition, as was shown in [58], the on-site EEI suppresses the charge fluctuation and reduces the absorbed energy. It is also expected that HHG yields suppression due to EEI. The latter is shown in Fig. 4, where the HHG spectra in the strong-field regime for different EEI energies are shown. To obtain the mean picture which does not depend on the orientation of the molecule with respect to laser polarization, we take the wave polarization unit vector as $\hat{e} = 1/\sqrt{3}\{1, 1, 1\}$. To make the plateaus more visible in Figs. 4(a) and 4(b) we show the envelopes of HHG spectra. As seen from Figs. 4(a) and 4(b), with the increase of the EEI energy overall the HHG rate is suppressed. Another interesting aspect of HHG in fullerene is the qualitative and quantitative difference between both molecules. As is seen, the C_{70} molecule shows more pronounced nonlinear properties [Fig. 4(c)]. Due to broken inversion symmetry in the case of C_{70} , we have even harmonics; in addition, due to the smaller energy gap and the larger density of states, the HHG rate is larger by one to two orders compared with C_{60} . For comparison, in Fig. 4(c) we show the first four plateaus for both molecules. The suppression of HHG with the increase of EEI energy is connected with the fact that at strong on-site and intersite electron-electron repulsion the polarizability of molecules, or in other words electrons migration from the equilibrium states, is suppressed. To show this visually, in Fig. 5 we display site occupations $n_i = \langle c_{i\uparrow}^\dagger c_{i\uparrow} \rangle + \langle c_{i\downarrow}^\dagger c_{i\downarrow} \rangle$ via three-dimensional (3D) color mapped molecular structures at the peak of the laser field for the z -polarized wave for the same interaction parameters. The color bar represents site occupation. As can be seen from Fig. 5, the deviation from the equilibrium position and, therefore, the polarization is maximum for vanishing EEI.

We also investigated the HHG spectra dependence versus pump wave frequency and intensity. In Figs. 6(a) and 6(b) we plot the HHG spectra versus pump wave frequency at moderate EEI energy $U = 2 \text{ eV}$, for C_{60} and C_{70} , respectively. For both molecules, the cutoff harmonic position is

well approximated by the dependence $N_{\text{cut}} \sim \omega^{-1/2}$ which is plotted along with density. Note that for atomic HHG via free continuum $N_{\text{cut}} \sim \omega^{-3}$ [6]. In the case of a two-level atom $N_{\text{cut}} \sim \omega^{-1}$ [59]. Thus, in contrast to atomic cases for a fullerene molecule, with the increase of the pump wave photon energy the cutoff harmonic energy ($\hbar\omega N_{\text{cut}}$) is increased.

Next, we consider the HHG spectra as a function of pump wave intensity. In Figs. 6(c) and 6(d), we show the HHG spectra as a function of field amplitude and the harmonic order for a fixed frequency. The HHG spectra have interesting structures. First of all, excitonic lines (marked by the white horizontal lines) are clearly seen. These excitonic lines define the borders of the plateaus and within each plateau, the cutoff harmonic linearly increases with increasing the field strength.

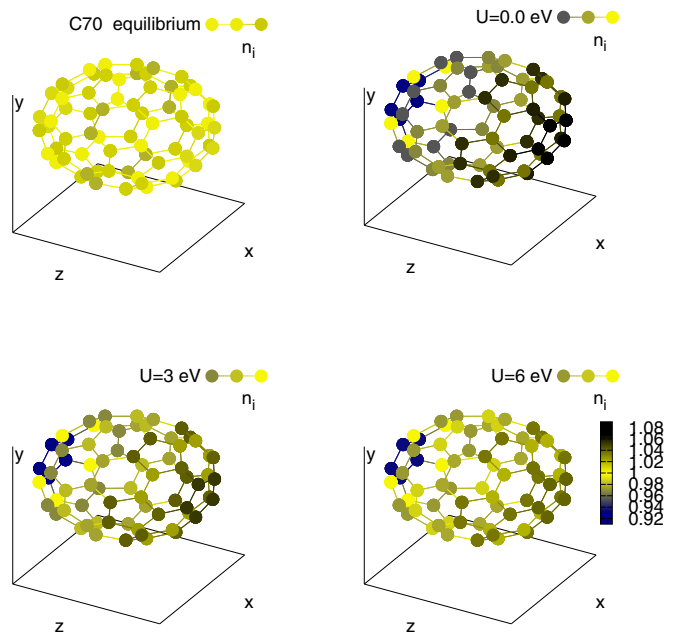


FIG. 5. The site occupations n_i in 3D color mapped molecular structures for C_{70} . The wave is assumed to be linearly polarized along the z axis. The first configuration is the equilibrium, the next three configurations are at the peak of the laser field $t = \mathcal{T}/2$ for different EEI energies.

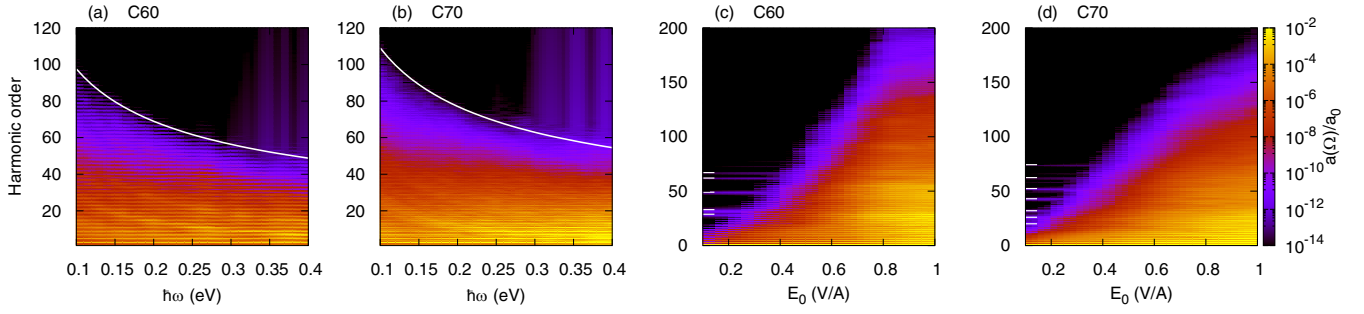


FIG. 6. The HHG spectra versus pump wave frequency (a),(b) and intensity (c),(d). The color bar represents the emission rate via dipole acceleration Fourier transformation $a(\Omega)/a_0$ in the logarithmic scale for C_{60} (a),(c) and C_{70} (b),(d). The wave is assumed to be linearly polarized with polarization unit vector $\hat{e} = \frac{1}{\sqrt{3}}\{1, 1, 1\}$. The field strength is fixed $E_0 = 0.5 \text{ V/\AA}$ for (a) and (b), while for (c) and (d) the frequency is fixed $\omega = 0.1 \text{ eV}/\hbar$. The spectra are shown for moderate EEI energy: $U = 2 \text{ eV}$. The relaxation rate is taken to be $\hbar\gamma = 50 \text{ meV}$. The white lines in (a) and (b) are envelopes $\alpha/\sqrt{\omega}$ which show the cutoff harmonic positions. The white horizontal lines in (c) and (d) are excitonic resonances that show each plateau's borders.

Then, reaching the harmonic ~ 160 which corresponds to the transition of the lowest occupied molecular orbital to the highest unoccupied molecular orbital, the HHG rate is saturated. Note that linear dependence of the cutoff harmonics on the field strength is inherent to HHG via discrete levels [59], or in crystals with linear energy dispersion [22,23,37].

We now consider the origin of the HHG in fullerene molecules. There are two contributions to the current: the electron/hole transitions within unoccupied/occupied molecular orbitals and the electron-hole creation (transitions from occupied molecular orbitals to unoccupied ones) and subsequent recombination. The former makes a contribution only for low harmonics and is analogous to the intraband current in a semiconductor, while the latter makes the main contribution in the high-frequency part and corresponds to the interband current, which represents recombination/creation of electron-hole pairs. This picture is analogous to HHG in solid state systems. To separate these contributions in the dipole acceleration spectrum we made a change of the basis via formula

$$\rho_{ij} = \sum_{\mu'} \sum_{\mu} \psi_{\mu'}^*(j) \rho_{\mu\mu'} \psi_{\mu}(i),$$

where $\rho_{\mu\mu'}$ is the density matrix in the energetic representation. Hence, we define the interband part of dipole

acceleration as

$$\mathbf{d}_{\text{inter}}(t) = 2 \sum_{\mu'=N/2}^{N-1} \sum_{\mu=0}^{N/2-1} \text{Re}(\rho_{\mu\mu'}(t) \mathbf{d}_{\mu'\mu}), \quad (5)$$

and the intraband part will be

$$\mathbf{d}_{\text{intra}}(t) = \sum_{\mu,\mu'=N/2}^{N-1} \rho_{\mu\mu'}(t) \mathbf{d}_{\mu'\mu} + \sum_{\mu,\mu=0}^{N/2-1} \rho_{\mu\mu'}(t) \mathbf{d}_{\mu'\mu}, \quad (6)$$

where the dipole transition matrix elements are $\mathbf{d}_{\mu'\mu} = e \sum_i \psi_{\mu'}^*(i) \mathbf{r}_i \psi_{\mu}(i)$. In Fig. 7(a), we show the interband/intraband contribution in HHG spectra for C_{60} . We have a similar picture for C_{70} . As is seen, intraband dipole acceleration is significant for the low-frequency part of the spectrum, while in the high-frequency part the main contribution is caused by the electron-hole creation and subsequent recombination. This information can also be extracted from the evolution of the high harmonic spectrum as a function of time. For this purpose a Blackman window of width $1.2\pi/\omega$ is scanned across 20 optical cycles. The results along with the population of the conduction band (unoccupied molecular orbitals) $W(t) = \sum_{\mu=0}^{N/2-1} \rho_{\mu\mu}(t)$ are displayed in Figs. 7(b) and 7(c). As seen from these figures, the emission

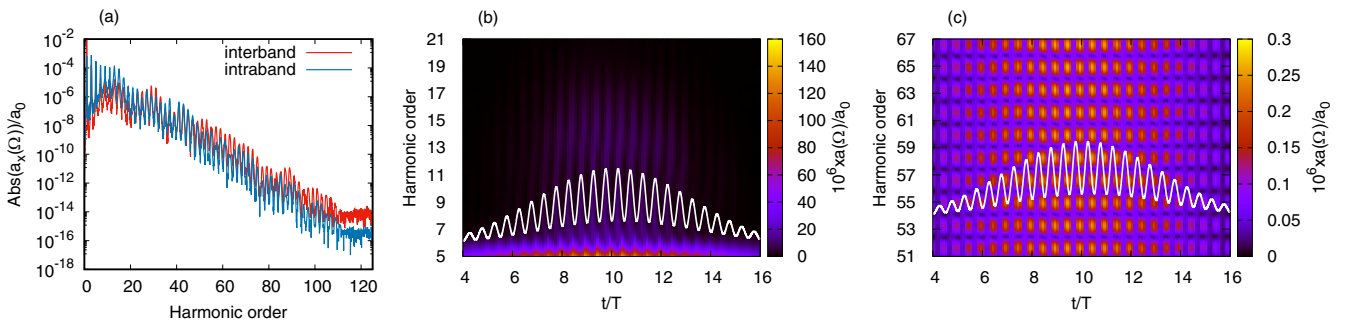


FIG. 7. The interband and intraband contribution in HHG spectra (a) and the spectrogram (b),(c) of the HHG process via the windowed Fourier transform of the dipole acceleration for C_{60} . The wave is assumed to be linearly polarized with polarization unit vector $\hat{e} = \frac{1}{\sqrt{3}}\{1, 1, 1\}$. The frequency is $\omega = 0.1 \text{ eV}/\hbar$ and the field strength is taken to be $E_0 = 0.5 \text{ V/\AA}$. The spectra are shown for $U = 2 \text{ eV}$ and $\hbar\gamma = 50 \text{ meV}$. (b) Low-frequency part and (c) high-frequency part. Then, the white curve on the density plots is scaled by the factor 10 population of the initially unoccupied molecular orbitals versus time.

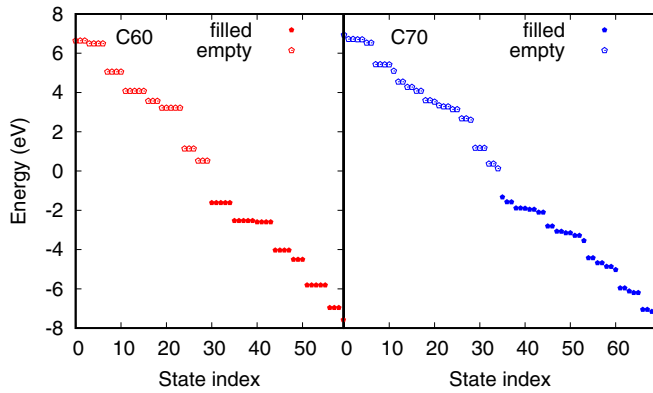


FIG. 8. The eigenenergies of fullerene molecules. The left and the right panels correspond to C₆₀ and C₇₀, respectively.

of high harmonics takes place two times per wave cycle, corresponding to two maxima or minima of the population. The low-frequency harmonic bursts take place in-between maxima and minima of the population Fig. 7(b), while higher harmonics are the result of the recombination and the bursts that take place at minima of the population [Fig. 7(c)]. There are also a domain of harmonics where we have an interplay between intra- and interband emission.

IV. CONCLUSION

We revealed the general features of the HHG in fullerene molecules under strong-field driving. The HHG spectra show multiple plateaus, which is explained by the recombination of electrons and holes from molecular orbitals. Those are intrinsic molecular excitations between the unoccupied molecular orbitals and the occupied molecular orbital. These intrinsic

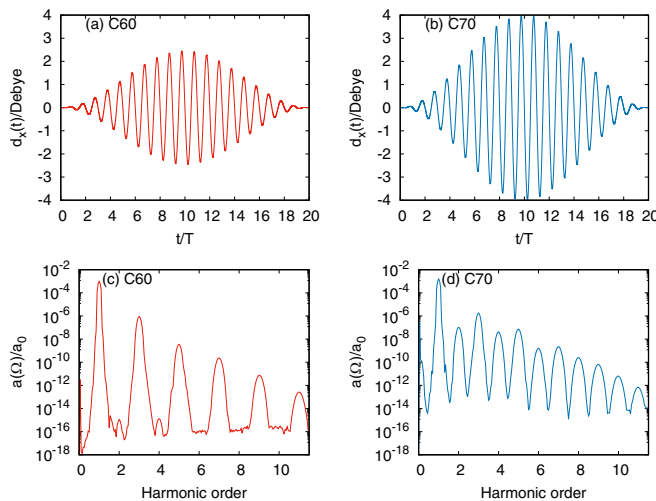


FIG. 9. The x component of the dipole moment versus time for C₆₀ (a) and for C₇₀ (b). The wave is assumed to be linearly polarized along the x axis. The frequency is $\omega = 0.1$ eV/ \hbar and the field strength is taken to be $E_0 = 0.1$ V/ \AA . The calculations are made for EEI energy $U = 2$ eV. Also shown are the corresponding HHG spectra (c) and (d) in logarithmic scale via the normalized dipole acceleration $\mathbf{a}(t) = d^2\mathbf{d}/dt^2$ Fourier transformation $a(\Omega)/a_0$.

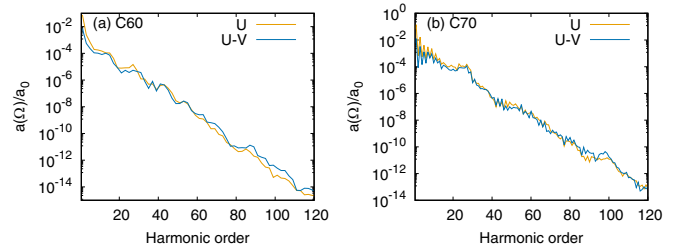


FIG. 10. The envelopes of HHG spectra in the strong-field regime for Hubbard ($V = 0$) and extended Hubbard ($V \neq 0$) models for C₆₀ (a) and C₇₀ (b). The frequency is $\omega = 0.1$ eV/ \hbar and the field strength is taken to be $E_0 = 0.5$ V/ \AA . The relaxation rate is taken to be $\hbar\gamma = 50$ meV. The wave polarization unit vector is $\hat{\mathbf{e}} = 1/\sqrt{3}\{1, 1, 1\}$.

molecular excitations, so-called excitonic lines, define the borders of the plateaus. Within each plateau, the cutoff harmonic linearly increases with increasing the field strength. In contrast to atomic cases, for fullerene molecules with the increase of the pump wave photon energy the cutoff harmonic energy is increased. The HHG spectra strongly depends on the molecule symmetry qualitatively as well as quantitatively. The C₇₀ molecule shows more pronounced nonlinear properties due to the degradation of molecular symmetry compared with C₆₀. We also revealed the role of EEI. With the increase of the EEI energy, overall the HHG rate is suppressed. The fullerene molecules are known to have different isomers with other point-group symmetries. Therefore, they are interesting systems as a new source of HHG, and spectroscopy based on HHG might be useful to reveal the symmetries and electron dynamics involved. Developing a detailed understanding of the HHG in different classes of fullerene molecules is an interesting topic for future work.

ACKNOWLEDGMENTS

This work was supported by the RA State Committee of Science in the frame of research Project No. 20TTWS-1C010.

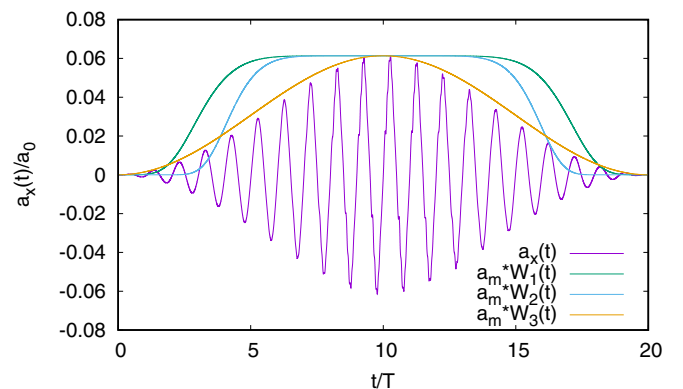


FIG. 11. The x component of the dipole acceleration versus time corresponding to Fig. 3(a) of the main text along with window functions with $\tau_1 = 300$ fs, $\tau_2 = 250$ fs, and $\tau_3 = 40/\omega = 263.28$ fs.

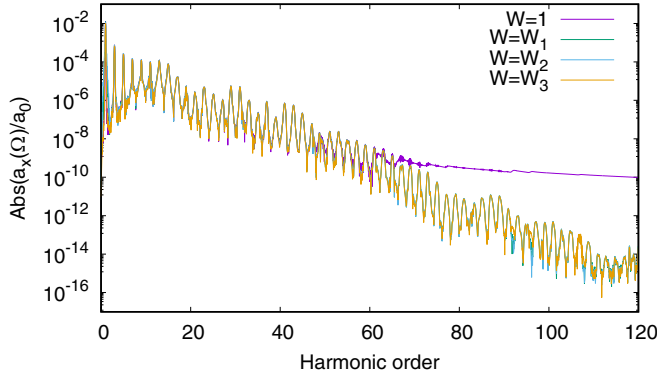


FIG. 12. The HHG spectrum calculated with various window functions corresponding to Fig. 3(a) of the main text.

APPENDIX A: MEAN-FIELD THEORY

In this Appendix, we clarify some details of used approximations, initial density matrix, and numerical integration. The free fullerene Hamiltonian of the main text can be written as

$$\begin{aligned} \hat{H}_0 = & - \sum_{(i,j)\sigma} t_{ij} c_{i\sigma}^\dagger c_{j\sigma} + \frac{U}{2} \sum_{i\sigma} c_{i\sigma}^\dagger c_{i\sigma} c_{i\bar{\sigma}}^\dagger c_{i\bar{\sigma}} \\ & + \frac{1}{2} \sum_{(i,j)\sigma\sigma'} V_{ij} c_{i\sigma}^\dagger c_{i\sigma} c_{j\sigma'}^\dagger c_{j\sigma'}. \end{aligned} \quad (\text{A1})$$

This is the extended Hubbard Hamiltonian with U and V terms included. Within the Hartree-Fock approximation, the Hamiltonian (A1) is approximated by

$$\begin{aligned} \hat{H}_0^{HF} = & - \sum_{(i,j)\sigma} t_{ij} c_{i\sigma}^\dagger c_{j\sigma} + U \sum_i (\bar{n}_{i\uparrow} - \bar{n}_{0i\uparrow}) n_{i\downarrow} \\ & + U \sum_{i\sigma} (\bar{n}_{i\downarrow} - \bar{n}_{0i\downarrow}) n_{i\uparrow} + \sum_{(i,j)} V_{ij} (\bar{n}_j - \bar{n}_{0j}) n_i \\ & - \sum_{(i,j)\sigma} V_{ij} c_{i\sigma}^\dagger c_{j\sigma} (\langle c_{i\sigma}^\dagger c_{j\sigma} \rangle - \langle c_{i\sigma}^\dagger c_{j\sigma} \rangle_0), \end{aligned} \quad (\text{A2})$$

where $\bar{n}_{i\sigma} = \langle c_{i\sigma}^\dagger c_{i\sigma} \rangle = \rho_{ii}^{(\sigma)}$. It is interesting to note the presence of an off-diagonal last term that renormalizes the transferred energy t_{ij} . In this representation the initial density matrix $\rho_{ji}^{(\sigma)} = \langle c_{i\sigma}^\dagger c_{j\sigma} \rangle_0$ is calculated with respect to tight-binding Hamiltonian $\hat{H}_0^t = - \sum_{(i,j)\sigma} t_{ij} c_{i\sigma}^\dagger c_{j\sigma}$. That is, in the static limit the EEI Hamiltonian vanishes, $\hat{H}_{ee}^{HF} \simeq 0$. It should be mentioned that EEI in the Hartree-Fock limit is included nonexplicitly in an empirical hopping integral between nearest-neighbor atoms t_{ij} which is chosen to be close to experimental values. Thus, EEI in the Hartree-Fock approximation is only relevant for the quantum dynamics initiated by the pump laser field. From the Heisenberg equation

$$i\hbar \partial \hat{L} / \partial t = [\hat{L}, \hat{H}_0^{HF} + \hat{H}_{int}] \quad (\text{A3})$$

one can obtain evolutionary equations for the single-particle density matrix, i.e., Eq. (4) of the main text. Thus, we have a set of nonlinear equations. The number of equations are 3600 and 4900 for C_{60} and C_{70} , respectively. For the numerical solution we need initial (equilibrium) $\rho_{0ij}^{(\sigma)}$ distribution. For this purpose we numerically diagonalize the tight-binding

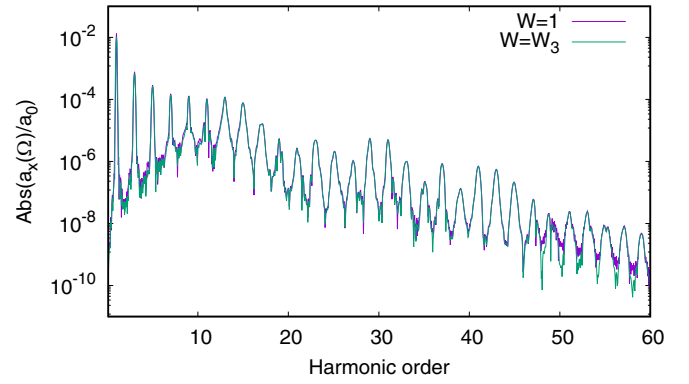


FIG. 13. The HHG spectrum calculated with and without window functions corresponding to Fig. 3(a) of the main text.

Hamiltonian \hat{H}_0^t . Input coordinates for C_{60} and C_{70} were generated with the program FULLERENE via a face-spiral algorithm [60]. This initial structure was further optimized by a force field specifically designed for fullerenes [61]. Then, the hopping integral between nearest-neighbor atoms at positions \mathbf{r}_i and \mathbf{r}_j is approximated as $t_{ij} = t_0 + \alpha(d_0 - |\mathbf{r}_i - \mathbf{r}_j|)$. Taking $d_0 = 1.54 \text{ \AA}$ and by fitting the energy gap for C_{60} and C_{70} , we have determined the average hopping constant $t_0 = 2.17 \text{ eV}$ and the electron-lattice coupling constant $\alpha = 3.52 \text{ eV/\AA}$. With the numerical diagonalization, we find eigenstates $\psi_\mu(i)$ and eigenenergies ε_μ ($\mu = 0, 1, \dots, N - 1$). The results of numerical diagonalization are shown in Fig. 8. As seen from this figure, compared with the C_{70} molecule, C_{60} has more degenerated states, which is a result of high symmetry. For the C_{60} molecule the highest occupied molecular orbital (HOMO) is at $E_{\text{HOMO}} = -1.61 \text{ eV}$, and the lowest unoccupied molecular orbital (LUMO) is at $E_{\text{LUMO}} = 0.52 \text{ eV}$. The next orbital where a dipole-allowed transition from HOMO is possible is at $E_{\text{LUMO}+1} = 1.13 \text{ eV}$. That is, the first dipole-allowed transition gap is $\Delta_g = 2.74 \text{ eV}$ with the averaged (over the degenerate states) transition dipole moment $d_m \simeq 4.3 \text{ D}$. For the C_{70} molecule these parameters are $E_{\text{HOMO}} = -1.32 \text{ eV}$, $E_{\text{LUMO}} = 0.13 \text{ eV}$, $E_{\text{LUMO}+1} = 0.37 \text{ eV}$, $\Delta_g = 1.69 \text{ eV}$, and $d_m \simeq 6.2 \text{ D}$. Note that the obtained gaps are reasonably close to widely accepted values [48,56,57,62].

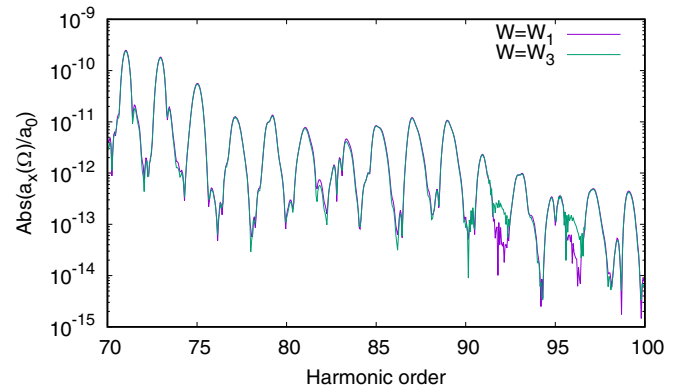


FIG. 14. The HHG spectrum calculated for two window functions near the end of the spectrum.

With the obtained eigenstates $\psi_{\mu}(i)$ we construct the initial density matrix and solve the equation of motion for the density matrix. The time integration of Eq. (4) of the main text is performed with the standard fourth-order Runge-Kutta algorithm. The time step is taken as $\Delta t = 2.5 \times 10^{-2}$ fs. At this time step, the results are converged since reducing the time step to $\Delta t = 1.25 \times 10^{-2}$ fs produces a negligible change in the solution. As an example, in Figs. 9(a) and 9(b) we plot the dipole moment $\mathbf{d}(t) = \langle e \sum_i \mathbf{r}_i n_i(t) \rangle$ versus time at a moderately strong laser field for C_{60} and C_{70} . As usual the fundamental harmonic is dominant and the time domain picture is not as informative as the Fourier picture. Hence, in Fig. 9 we also show the HHG spectra. As expected for C_{60} because of the inversion symmetry, only odd harmonics appear in the HHG spectrum. For the C_{70} molecule we have both even and odd harmonics.

In addition, in Fig. 10, we also compared the relative contributions of the U and V terms of the EEI to the HHG spectra for the same parameters as in Fig. 4 of the main text. As can be seen from this figure in this range of interaction parameters, namely, at $\hbar\omega \ll t_{ij}, U$, the results qualitatively coincide, although there is a quantitative difference.

APPENDIX B: FILTERED FOURIER TRANSFORMATION

Next, we would like to explain how Fourier transformation is carried out. The filtered Fourier transformation is necessary since there are very small oscillations at the beginning and at the end of the time evolution. They increase the overall background (noise level) of the harmonic signal, which smears harmonic signals near the cutoff. The intense HHG takes place for the peak values of the laser field. Thus, a window function is required to suppress small fluctuations [63]. The harmonic

signal is computed by Fourier transformation

$$\mathbf{a}(\Omega) = \int_0^{\mathcal{T}} \mathbf{a}(t) e^{i\Omega t} W(t) dt,$$

where $W(t)$ is the window function.

Note that using the window function does not change the rate of harmonics [63], which is verified in our calculation. We take Fig. 3(a) of the main text as an example. For Fourier transformation, we use the FFTW [64] subroutine library. In Fig. 11 we plot $a(t)/a_0$ corresponding to Fig. 3(a) and window functions [rescaled to a maximum of $a(t)$]. We use three window functions: hyper-Gaussian

$$W_{1,2}(t) = \exp \left\{ - \left(\frac{t - \mathcal{T}/2}{\tau_{1,2}} \right)^8 \right\}$$

with different parameters $\tau_{1,2}$, and squared sine window

$$W_3 = \sin^2 \left(\frac{t}{\tau_3} \right).$$

In Fig. 12 we plot the HHG spectrum for these window functions along with direct Fourier transform. We see that if we do not use the window function, the spectrum has harmonics only up to the 65th order, with a big background. With the window functions, the original strong background is removed, and higher harmonics' peaks show up. Note that harmonic rates are independent of window functions. For a more detailed view, in Fig. 13 we plot the direct Fourier transform spectrum and the spectrum with W_3 up to the 60th harmonic. We see that the window function has a negligible effect on the HHG spectrum. For a closer look, in Fig. 14 we plot the spectrum for two window functions near the end of the spectrum. We see that for both window functions the spectra are almost the same. One can equally use one of the mentioned functions. We used W_3 for the main text.

-
- [1] H. K. Avetissian, *Relativistic Nonlinear Electrodynamics: The QED Vacuum and Matter in Super-Strong Radiation Fields* (Springer, Berlin, 2015).
- [2] A. Di. Piazza, C. Müller, K. Z. Hatsagortsyan, and C. H. Keitel, *Rev. Mod. Phys.* **84**, 1177 (2012).
- [3] P. Agostini and L. F. DiMauro, *Rep. Prog. Phys.* **67**, 813 (2004).
- [4] M. C. Kohler, T. Pfeifer, K. Z. Hatsagortsyan, and C. H. Keitel, *Adv. At. Mol., Opt. Phys.* **61**, 159 (2012).
- [5] P. B. Corkum, *Phys. Rev. Lett.* **71**, 1994 (1993).
- [6] M. Lewenstein, P. Balcou, M. Y. Ivanov, A. L'Huillier, and P. B. Corkum, *Phys. Rev. A* **49**, 2117 (1994).
- [7] P. B. Corkum and F. Krausz, *Nat. Phys.* **3**, 381 (2007).
- [8] F. Krausz and M. Ivanov, *Rev. Mod. Phys.* **81**, 163 (2009).
- [9] H. Lakhota, H. Y. Kim, M. Zhan, S. Hu, S. Meng, and E. Goulielmakis, *Nature (London)* **583**, 55 (2020).
- [10] R. E. F. Silva, I. V. Blinov, A. N. Rubtsov, O. Smirnova, and M. Ivanov, *Nat. Photonics* **12**, 266 (2018).
- [11] D. Bauer and K. K. Hansen, *Phys. Rev. Lett.* **120**, 177401 (2018).
- [12] G. Vampa, T. J. Hammond, N. Thiré, B. E. Schmidt, F. Légaré, C. R. McDonald, T. Brabec, D. D. Klug, and P. B. Corkum, *Phys. Rev. Lett.* **115**, 193603 (2015).
- [13] N. Tancogne-Dejean, O. D. Mücke, F. X. Kartner, and A. Rubio, *Phys. Rev. Lett.* **118**, 087403 (2017).
- [14] C. G. Wahlstram, J. Larsson, A. Persson, T. Starczewski, S. Svanberg, P. Salieres, P. Balcou, and A. L'Huillier, *Phys. Rev. A* **48**, 4709 (1993).
- [15] T. D. Donnelly, T. Ditmire, K. Neuman, M. D. Perry, and R. W. Falcone, *Phys. Rev. Lett.* **76**, 2472 (1996).
- [16] C. Vozzi, M. Nisoli, J. Caumes, G. Sansone, S. Stagira, S. De Silvestri, M. Vecchiocattivi, D. Bassi, M. Pascolini, L. Poletto, P. Villoresi, and G. Tondello, *Appl. Phys. Lett.* **86**, 111121 (2005).
- [17] O. Smirnova, Y. Mairesse, S. Patchkovskii, N. Dudovich, D. Villeneuve, P. Corkum, and M. Yu. Ivanov, *Nature (London)* **460**, 972 (2009).
- [18] S. Ghimire, A. D. DiChiara, E. Sistrunk, P. Agostini, L. F. DiMauro, and D. A. Reis, *Nat. Phys.* **7**, 138 (2011).
- [19] B. Zaks, R. B. Liu, and M. S. Sherwin, *Nature (London)* **483**, 580 (2012).
- [20] F. Langer, M. Hohenleutner, C. P. Schmid, C. Poellmann, P. Nagler, T. Korn, C. Schüller, M. S. Sherwin, U. Huttner, J. T. Steiner, S. W. Koch, M. Kira, and R. Huber, *Nature (London)* **533**, 225 (2016).

- [21] O. Schubert, M. Hohenleutner, F. Langer, B. Urbanek, C. Lange, U. Huttner, D. Golde, T. Meier, M. Kira, S. W. Koch, and R. Huber, *Nat. Photonics* **8**, 119 (2014).
- [22] G. Vampa, C. R. McDonald, G. Orlando, D. D. Klug, P. B. Corkum, and T. Brabec, *Phys. Rev. Lett.* **113**, 073901 (2014).
- [23] G. Vampa, C. R. McDonald, G. Orlando, P. B. Corkum, and T. Brabec, *Phys. Rev. B* **91**, 064302 (2015).
- [24] G. Ndashimiye, S. Ghimire, M. Wu, D. A. Browne, K. J. Schafer, M. B. Gaarde, and D. A. Reis, *Nature (London)* **534**, 520 (2016).
- [25] Y. S. You, D. A. Reis, and S. Ghimire, *Nat. Phys.* **13**, 345 (2017).
- [26] H. Liu, C. Guo, G. Vampa, J. L. Zhang, T. Sarmiento, M. Xiao, P. H. Bucksbaum, J. Vuckovic, S. Fan, and D. A. Reis, *Nat. Phys.* **14**, 1006 (2018).
- [27] S. A. Mikhailov and K. Ziegler, *J. Phys.: Condens. Matter* **20**, 384204 (2008).
- [28] H. K. Avetissian, A. K. Avetissian, G. F. Mkrtchian, and K. V. Sedrakian, *Phys. Rev. B* **85**, 115443 (2012).
- [29] H. K. Avetissian, G. F. Mkrtchian, K. G. Batrakov, S. A. Maksimenko, and A. Hoffmann, *Phys. Rev. B* **88**, 165411 (2013).
- [30] P. Bowlan, E. Martinez-Moreno, K. Reimann, T. Elsaesser, and M. Woerner, *Phys. Rev. B* **89**, 041408(R) (2014).
- [31] I. Al-Naib, J. E. Sipe, and M. M. Dignam, *Phys. Rev. B* **90**, 245423 (2014).
- [32] H. K. Avetissian and G. F. Mkrtchian, *Phys. Rev. B* **94**, 045419 (2016).
- [33] L. A. Chizhova, F. Libisch, and J. Burgdorfer, *Phys. Rev. B* **95**, 085436 (2017).
- [34] D. Dimitrovski, L. B. Madsen, and T. G. Pedersen, *Phys. Rev. B* **95**, 035405 (2017).
- [35] N. Yoshikawa, T. Tamaya, and K. Tanaka, *Science* **356**, 736 (2017).
- [36] H. K. Avetissian and G. F. Mkrtchian, *Phys. Rev. B* **97**, 115454 (2018).
- [37] H. K. Avetissian, A. K. Avetissian, B. R. Avchyan, and G. F. Mkrtchian, *Phys. Rev. B* **100**, 035434 (2019).
- [38] H. K. Avetissian and G. F. Mkrtchian, *Phys. Rev. B* **99**, 085432 (2019).
- [39] H. Liu, Y. Li, Y. S. You, S. Ghimire, T. F. Heinz, and D. A. Reis, *Nat. Phys.* **13**, 262 (2017).
- [40] H. K. Avetissian, G. F. Mkrtchian, and K. Z. Hatsagortsyan, *Phys. Rev. Research* **2**, 023072 (2020).
- [41] G. Le Breton, A. Rubio, and N. Tancogne-Dejean, *Phys. Rev. B* **98**, 165308 (2018).
- [42] H. W. Kroto, J. R. Heath, S. C. O'Brien, R. F. Curl, and R. E. Smalley, *Nature (London)* **318**, 162 (1985).
- [43] W. Krätschmer, L. Lamb, K. Fostiropoulos, and D. R. Huffman, *Nature (London)* **347**, 354 (1990).
- [44] S. Iijima, *Nature (London)* **354**, 56 (1991).
- [45] A. K. Geim and I. V. Grigorieva, *Nature (London)* **499**, 419 (2013).
- [46] R. A. Ganeev, L. B. Elouga Bom, J. Abdul-Hadi, M. C. H. Wong, J. P. Brichta, V. R. Bhardwaj, and T. Ozaki, *Phys. Rev. Lett.* **102**, 013903 (2009).
- [47] R. A. Ganeev, L. B. Elouga Bom, M. C. H. Wong, J.-P. Brichta, V. R. Bhardwaj, P. V. Redkin, and T. Ozaki, *Phys. Rev. A* **80**, 043808 (2009).
- [48] G. P. Zhang, *Phys. Rev. Lett.* **95**, 047401 (2005).
- [49] G. P. Zhang and T. F. George, *Phys. Rev. A* **74**, 023811 (2006).
- [50] G. P. Zhang and T. F. George, *J. Opt. Soc. Am. B* **24**, 1150 (2007).
- [51] G. P. Zhang and Y. H. Bai, *Phys. Rev. B* **101**, 081412(R) (2020).
- [52] R. L. Martin and J. P. Ritchie, *Phys. Rev. B* **48**, 4845 (1993).
- [53] G. P. Zhang, *Phys. Rev. B* **56**, 9189 (1997).
- [54] G. P. Zhang, *Phys. Rev. B* **61**, 4377 (2000).
- [55] G. Chiappe, E. Louis, E. San-Fabian, and J. A. Verges, *J. Phys.: Condens. Matter* **27**, 463001 (2015).
- [56] R. W. Lof, M. A. van Veenendaal, B. Koopmans, H. T. Jonkman, and G. A. Sawatzky, *Phys. Rev. Lett.* **68**, 3924 (1992).
- [57] T. Rabenau, A. Simon, R. K. Kremer, and E. Sohmen, *Z. Phys. B* **90**, 69 (1993).
- [58] G. P. Zhang, *Phys. Rev. Lett.* **91**, 176801 (2003).
- [59] H. K. Avetissian, B. R. Avchyan, and G. F. Mkrtchian, *J. Phys. B* **45**, 025402 (2012).
- [60] P. W. Fowler and D. E. Manolopoulos, *An Atlas of Fullerenes* (Dover, New York, 2006).
- [61] P. Schwerdtfeger, L. Wirz, and J. Avery, *J. Comput. Chem.* **34**, 1508 (2013).
- [62] E. L. Shirley and S. G. Louie, *Phys. Rev. Lett.* **71**, 133 (1993).
- [63] G. P. Zhang, M. S. Si, M. Murakami, Y. H. Bai, and T. F. George, *Nat. Commun.* **9**, 3031 (2018).
- [64] <https://www.fftw.org>.